A negative-response strain sensor towards wearable microclimate changes for body area sensing networks

Jing Liu[a], Junze Zhang[a], Zeyu Zhao[a], Yanping Liu[b], Wai Cheong Tam[c], Zhaozhu Zheng[a], Xiaoqin Wang[a], Yuling Li[b], Zekun Liu[d, e], Yi Li[d], Gang Li[a*]

[a] National Engineering Laboratory for Modern Silk, Soochow University, Suzhou 215123, China.
[b] Key Laboratory of Textile Science and Technology, Ministry of Education, Donghua University, Shanghai, 201620, China.
[c] Fire Research Division, National Institute of Standards and Technology, Gaithersburg, MD 20899.
[d] Department of Materials, The University of Manchester, Oxford Road, Manchester M13 9PL, UK.
[e] Botnar Research Center, University of Oxford, Old Road, Headington, Oxford OX3 7LD.

Abstract: Wearables and strain sensors have attracted much attention for applications in monitoring human motions and health. However, state-of-the-art sensors lack sensing reliability in changing temperature and humidity conditions. In this study, we design and fabricate a robust strain sensor using silk/polyurethane composite yarns. The silk is modified using graphene with the assistance of 3-glycidyloxypropyl trimethoxy silane as coupling agent. The sensor is durable and has fast response speed, stable sensing capability, and a robust resistance response towards strain deformation. More importantly, the sensor performance will not be affected by changing temperature and humidity in typical use conditions. The sensor is used to further develop a real-time body sensing network. Results from this study show that the fabricated strain sensor has huge potential for future personalized healthcare and public health management.

Keywords: strain sensor, fiber functionalization, graphene, wearable microclimate, body sensing networks

1. Introduction

Immense amounts of research on wearable sensing devices have greatly expanded the horizons of personal and public health management [1-4]. Simple strain sensors offer high flexibility and high sensing performance. Due to its unique material behaviors, strain sensors also provide great potential in physiological signal detection [5-8]. Carbon nanotubes, polyaniline, metal nanoparticles and graphene are commonly used as active materials to provide electrical conductivity for sensors [9-12]. Compared to other materials, graphene, a two-dimensional hexagonal structural material composed of sp^2-bonded carbon atoms, is an excellent candidate for the fabrication of flexible skin-mountable strain sensors because of its higher aspect ratios, superior electrical and mechanical properties, and preferable chemical stability [13]. Although strain sensors with graphene modification have been extensively studied [14-17], the existing strain sensors have weak strengths and/or unstable bonding in between the substrate and the graphene. For that, it is important to explore an effective strategy to increase the coating firmness to improve the sensing reliability for practical use scenarios.

Depending on different activity levels, human bodies generally produce about 60 ml to 840 mL of sweat per hour [11]. Even at rest, physical breathing occurs on the skin surface and sweat in the form of water vapor evaporates from the skin. Similarly, the skin temperature also changes as a function of metabolic intensity and sweat evaporation. For that, wearable sensors need to have reliable sensing capabilities in dynamic temperature and humidity environments [18, 19]. However, the current state-of-the-art sensors are not designed to be used in such practical environments and their sensing performance is unstable when the temperature and humidity are continuously changing [20, 21].

Therefore, it is highly desirable to develop a robust and reliable on-skin strain sensor that can obtain signals due to any body movements in various temperature and humidity conditions.

In this paper, we propose a silk yarn-like strain sensor with a core-sheath structure, where the elastic core fibers and the graphene-modified sheath fibers serve as mechanical and active components, respectively [22, 23]. The silk yarn does not only have high flexibility and mechanical strength, but it also provides high biocompatibility and sustainability, which can be a potential material for wearable devices. As a polymer composed of amino acids, silk has multiple reactive groups on its surface that can serve as reaction sites [24]. The bonding between the graphene and the silk fibers in hydroxyl groups, carbonyl groups, and epoxide groups can be enhanced using 3-glycidyloxypropyl trimethoxy silane as a coupling agent (CA). The sensor made with the silk/Polyurethane (PU) composite yarn (SPY) reveals a unique resistance response upon tensile strain and a stable sensing capability in a wide range of temperature and humidity conditions. In the following sections, material functionalization and sensor fabrication will be presented. Results will be provided. Since our goal is to eventually implement the new strain sensor in real-life applications, a real-time body sensing network is developed to demonstrate the usefulness of the sensor with different activities and motions. It is hoped that the fabricated sensor can help to enable future digital healthcare.

2. Experimental Section

2.1. Material functionalization and sensor fabrication

Fig. 1 shows the procedure for the fabrication of the sensor. There are four major steps: 1) silk yarn (SY) and PU filaments are first pre-drawn with tensioners and they are then fed into a roller

simultaneously. The two mixed groups of yarns (SY and PU) are twisted together to form the silk/PU composite yarn (SPY). After the loading pre-drawn is released, the PU filament is retracted to its original length making the silk yarn to form a core-sheath structure around the PU core filament. This allows the SPY to be prepared. 2) The SPY is modified by a coupling agent (CA). First, the yarn is ultrasonically cleaned with deionized water at ~ 60°C for about 30 mins. Then, the treated yarn is immersed into water and 3-(2, 3-epoxypropyl) propyl trimethoxy silane solution with the silane and water ratio of 1:30 at ~ 60 °C for approximately 4 hours. The dried yarn becomes the CA-assisted SPY (CA-SPY). 3) The CA-SPY will be treated with a graphene oxide (GO) solution. The GO solution is prepared using the modified Hummer's method based on [11, 25]. Approximately 2 g of graphite powders, 2 g of $NaNO_3$, and 50 mL of H_2SO_4 are mixed in a container and stirred in a constant speed for about 2 hours. Afterward, approximately 6 g of $KMnO_4$ is gradually added to the mixture with the temperature of the solution maintaining below 5 °C. Then, the mixture is stirred for about 2 days. Next, ~ 100 mL of water and ~ 10 mL of H_2O_2 are added to terminate the reaction. The mixture was washed and rinsed in a centrifuge using 10 % HCl and deionized water. With that, the GO solution with uniform dispersion is obtained. After that, the yarn is soaked in the GO dispersion for about 1 hour and the unwanted GO liquid is removed by using a small rolling mill with a pressure of ~ 0.2 MPa. This cycle is repeated 9 times. And finally, the yarn is dried at 60 °C to achieve the GO modification. 4) Ascorbic acid is used to reduce GO [26] on the surface of the yarn. The yarn is submerged into the 80 °C ascorbic acid for approximately 24 hours and the CA-SPY with reduced GO (rGO) is obtained. The final yarn is denoted as CA-rGSPY. In order to complete the strain sensor, the CA-rGSPY is cut into about 5 cm segments and the two leading edges are attached to two conducting wires using silver paste. This forms the CA-rGSPY strain sensor.

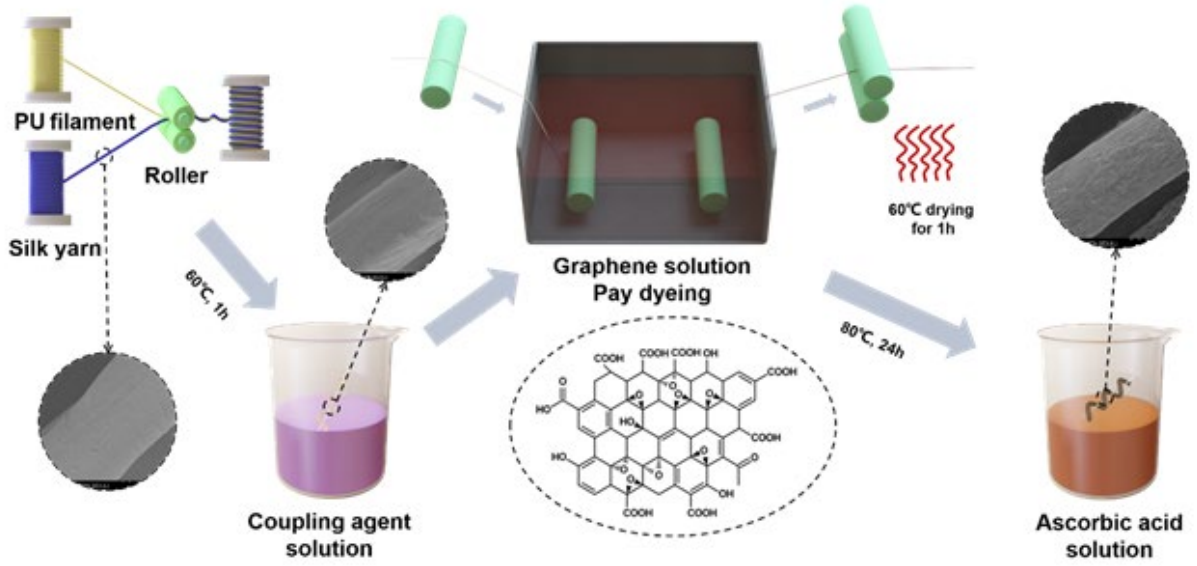

Fig. 1. Schematic diagram of fabrication of the CA-rGSPY

2.2. Morphology and structure characterization

Surface morphologies of the sensor are obtained using a Scanning Electron Microscope (SEM). The element content and distribution are obtained using a desktop SEM. A Fourier transform infrared spectroscopy with a 532 nm laser wavelength is utilized to examine the secondary structure features of the sensor. Crystalline phases are investigated using X-ray Powder in Co Kα radiation (λ = 1.5418 Å) at the 2θ ranging from 5 ° to 50 °. Thermogravimetric analysis of the sensor is also performed.

2.3. Evaluation of electromechanical performance and reliability

Mechanical performance is assessed utilizing a universal material testing machine. The tensile properties of the yarn with a gauge length of ~ 50 mm are measured in accordance with ASTM D2653. The pre-tensioning force value is about 0.3 cN with a crosshead speed of ~ 500 mm/min. The surface resistance of the sensor is measured using a digital multimeter. We washed the sensors in a beaker with laundry liquid with a magnetic stirrer at ambient temperature. Tension to the sensors is applied using

a tensile module. The electrical signals generated by the sample/strain sensor are collected by a multimeter and a programmable software. Assessments for relative humidity and temperature stability of the sensor are performed in an enclosed electrochemical shielding box. Using a humidifier, moisture was injected into the box to increase the relative humidity. In order to create an elevated temperature condition, heated air was blown into the box.

3. Results and discussion

3.1. Characterizations of the CA-rGSPY

Fourier transform infrared (FTIR) spectra of SPY, CA-SPY, rGSPY, and CA-rGSPY are depicted in Fig. 2a. As shown in the figure, there is a general difference for the absorptance at 1040 cm^{-1} and 906 cm^{-1} and this spectral behavior corresponds to the stretching vibrations of Si-O-Si and the rocking vibrations of Si-C in the silane coupling agent [27, 28]. The new peaks in the CA-SPY and CA-rGSPY are attributed to the deposition of the CA on the silk surface. For quantifying the conformational changes in the secondary structure caused by the interactions between the silk fibroin and the CA from the functionalization process, we deconvolve the FTIR spectra for both SPY and CA-SPY in the amide I zone (1600 cm^{-1} to 1500 cm^{-1}) (see Fig. 2b and 2c) [29]. It is found that the β-sheet structure in the secondary structure is significantly improved. This means that the CA is likely to be the primary cause of the β-sheet produced by silk fibroin, which can be induced by hydrogen bond between CA and silk as shown in Fig. 2d [30]. On the other hand, this modification does not deteriorate the uniform distribution of elements and there is the presence of Si on the surface of CA-SPY, CA-GSPY and CA-rGSPY after the CA coating is applied.

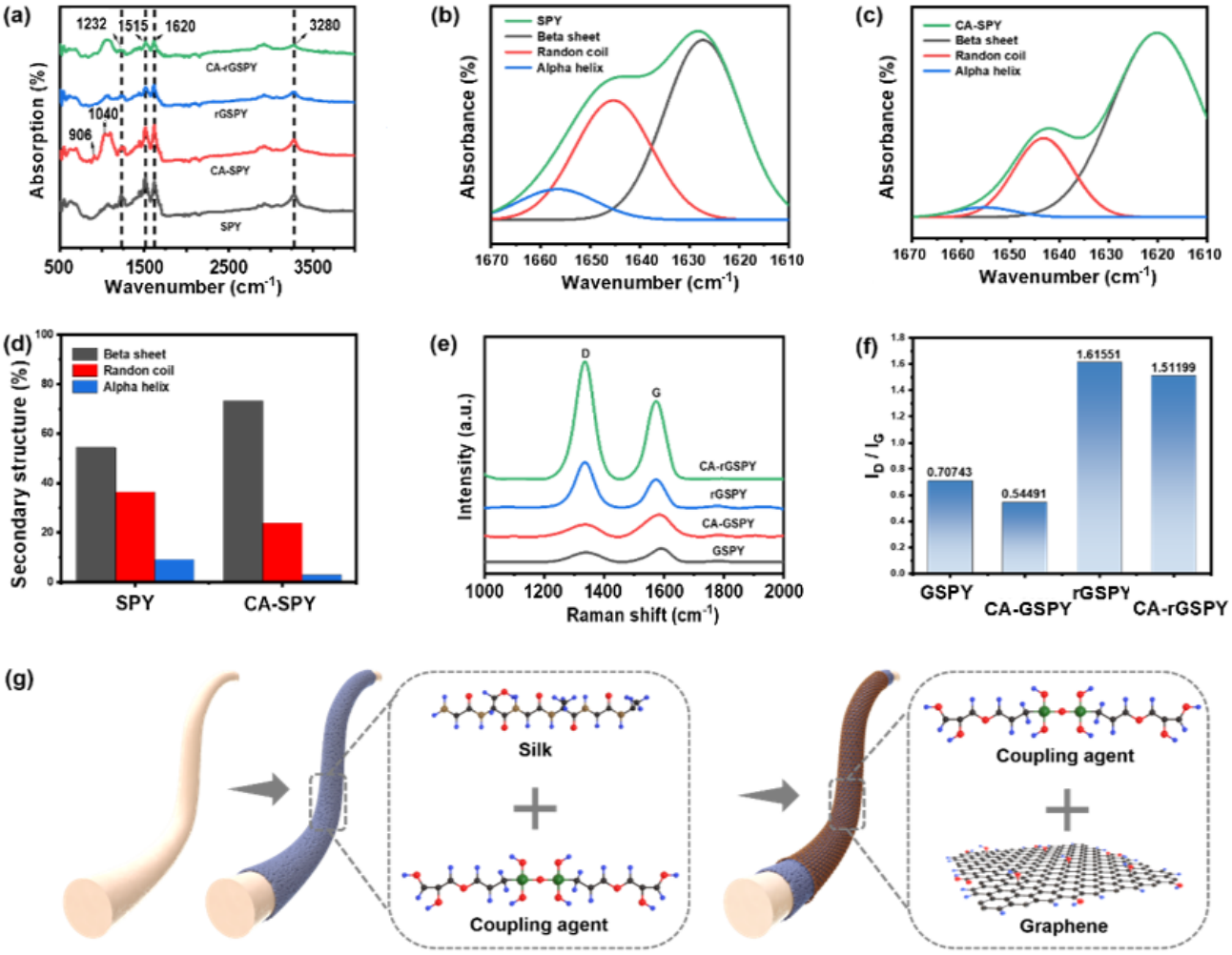
(a)
1232
1515
1620
3280
1040
906
CA-rGSPY
rGSPY
CA-SPY
SPY
Absorption (%)
500
1500
2500
3500
Wavenumber (cm-1)
(b)
SPY
Beta sheet
Randon coil
Alpha helix
Absorbance (%)
1670
1660
1650
1640
1630
1620
1610
Wavenumber (cm-1)
(c)
CA-SPY
Beta sheet
Randon coil
Alpha helix
Absorbance (%)
1670
1660
1650
1640
1630
1620
1610
Wavenumber (cm-1)
(d)
Beta sheet
Randon coil
Alpha helix
Secondary structure (%)
100
80
60
40
20
0
SPY
CA-SPY
(e)
D
G
CA-rGSPY
rGSPY
CA-GSPY
GSPY
Intensity (a.u.)
1000
1200
1400
1600
1800
2000
Raman shift (cm-1)
(f)
1.61551
1.51199
0.70743
0.54491
ID / IG
GSPY
CA-GSPY
rGSPY
CA-rGSPY
(g)
Silk
Coupling agent
Coupling agent
Graphene

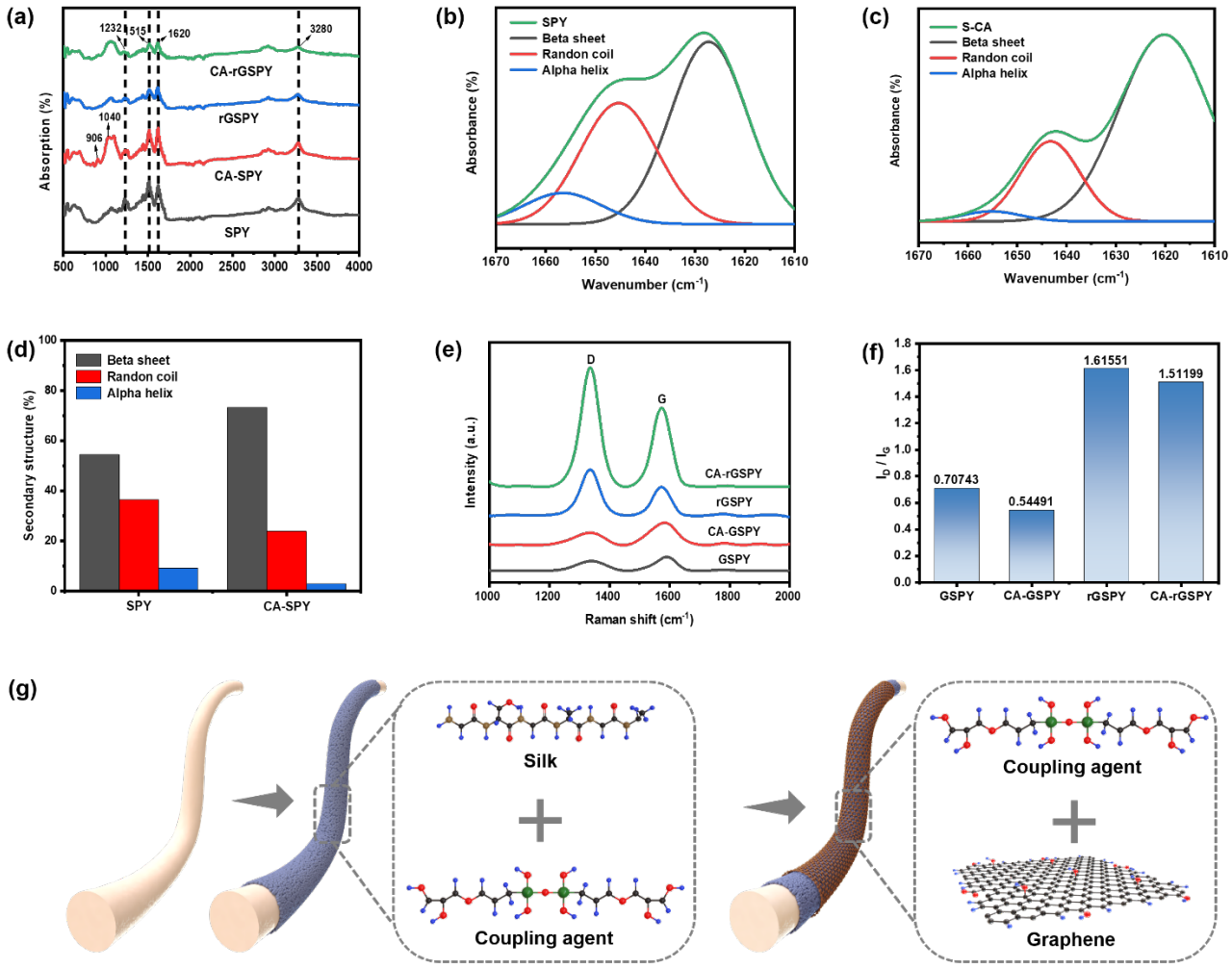

Fig. 2. Characterization of the SPYs. a) FTIR spectra of the SPY, CA-SPY, rGSPY, CA-rGSPY. The deconvolved FTIR spectra of b) the SPY, and c) the CA-SPY. d) Conformational changes in secondary structures of the SPY, CA-SPY. e) Raman spectra of the GSPY, CA-GSPY, rGSPY, CA-rGSPY with a.u. meaning arbitrary unit. f) I_D/I_G values calculated from Raman spectra. g) Schematic diagrams of the bonding mechanism between layers on the CA-rGSPY surface.

The surface of both SPY and CA-SPY is generally smooth with uniform wrinkles. The winkles are formed because both SPY and CA-SPY were treated with graphene. By analyzing the surface element contents, it is found that the percentage of O in the GSPY and the CA-GSPY decreases as a function of reducing presence of graphene, which is consistent with the previous work [31] . Raman spectra of GSPY, CA-GSPY, rGSPY, and CA-rGSPY are shown in Fig. 2e and it shows the reduction of rGO from the GO on the fiber surface. Two distinct peaks are observed at 1336 cm^{-1} and 1573 cm^{-1} in which

correspond to the Disorder Induced Mode (D) and Tangential Mode (G), respectively [32]. The initiate I_D/I_G value of GSPY and CA-GSPY is 0.70743 and 0.54491, respectively. After the application of rGO, the I_D/I_G values increase to 1.61551 and 1.51199 as show in Fig. 2f. This increase is attributed to the structural defects and disorders of the in-plane carbon network induced by the GO reduction. Because of the structural defects, the sp^2 domain is reduced in size and is transited from sp^2 to sp^3 [33]. On the other hand, the I_D/I_G values of the CA-GSPY (0.5491) are lower than that of the GSPY (0.70743). This is mainly because the remaining hydroxyl group on the CA bonds to the epoxy group of GO [34].

Based on the abovementioned analysis, a schematic model of the bonding mechanism between layers on the CA-rGSPY surface is constructed and is illustrated in Fig. 2g. The increase of β-sheet structure indicates that the carbonyl groups (appeared in amino acids of silk) react with the hydroxyl groups (appeared in CA) and is bound by forming the hydrogen bonds. The decrease in I_D/I_G values of GO is caused by the partly disappearance of oxygen-containing functional groups and this observation provides the reason why tight binding of CA with GO is the substitution reaction between hydroxyl groups and oxygen-containing functional groups of GO. It is seen that the characteristic peaks, which are attributed to the crystal structure of silk fibroin (Silk II), of all samples at different 2θ (i.e., ≈ 20.34 °, 24.6 ° and 29.6 °) [35]. No significant difference is observed and this result indicates that the crystal structure of silk is not being destroyed during the functionalization. It is also found that the thermal stability of the samples. When the temperature rises from 50 °C to 550 °C, the weight loss rate reaches about 60 % for all samples. However, the samples coated with the CA and modified by graphene show slightly less weight deterioration due to heating.

To investigate the relationship between the sensor resistance and the functional coating cyclicality, three pad dyeing settings (3, 6 and 9 times) are considered and the yarns (CA-rGSPY) are denoted as the CA-rGSPY3, CA-rGSPY6, and CA-rGSPY9, respectively. Fig. 3a shows the average resistivity of each setting and it dramatically decreases with the increasing dyeing cycles. In the same figure, the resistivity of the CA-rGSPY is shown to be lower than that of rGSPY and this indicates that presence of CA improves the performance in electrical conductivity [36]. To measure the conductivity stability in practical conditions, the rGSPY and the CA-rGSPY are washed using laundry liquid. With increasing washing time (Fig. 3b) and cycles (Fig. 3c), the change of the average resistivity of CA-rGSPY is much less as compared to that of rGSPY and this observation suggests that the use of CA offers prominent coating fastness. The conductivity of CA-rGSPY can be illustrated by applying low voltage onto the embedded LED bulbs as shown in Figs. 3d-3f. The LED bulb from the CA-rGSPY9 appears to be the brightest, revealing its robustness in conductivity.

It is worth emphasizing that silk, but not the PU, plays the role of conducting electricity in the CA-rGSPY and it can be seen that there is no wrinkled graphene structure on the PU surface after modification (see Fig. 3g). This is because the surface of the PU is smooth and lacks active functional groups to bind graphene. It can be seen in Figs. 3h that the silk yarn is generally conductive and the PU is not conductive (see Fig. 3i). Typical tensile strain curves of SPY and CA-rGSPY are shown in Fig. 3j. The pristine yarn possesses a strain limit of 124% and the CA-rGSPY3, CA-rGSPY6, CA-rGSPY9 has a strain limit of 125 %, 128 % and 131 %, respectively. The slight increase in strain limit is attributed by the shrink of the PU from the reduction (rGO). Although the PU is not conductive, it can offer improved elongation which makes the yarn highly stretchable (Fig. 3k). However, with the

loose and inelastic silk fibers in the yarn under the high tensile action, the stress increases significantly after reaching a certain strain (from the helical state to the straight state). As the strain gradually increases and exceeds the tolerable strain, the stretched silk fibers begin to break (Fig. 3l) [37, 38] and this observation is consistent with the previous work [39].

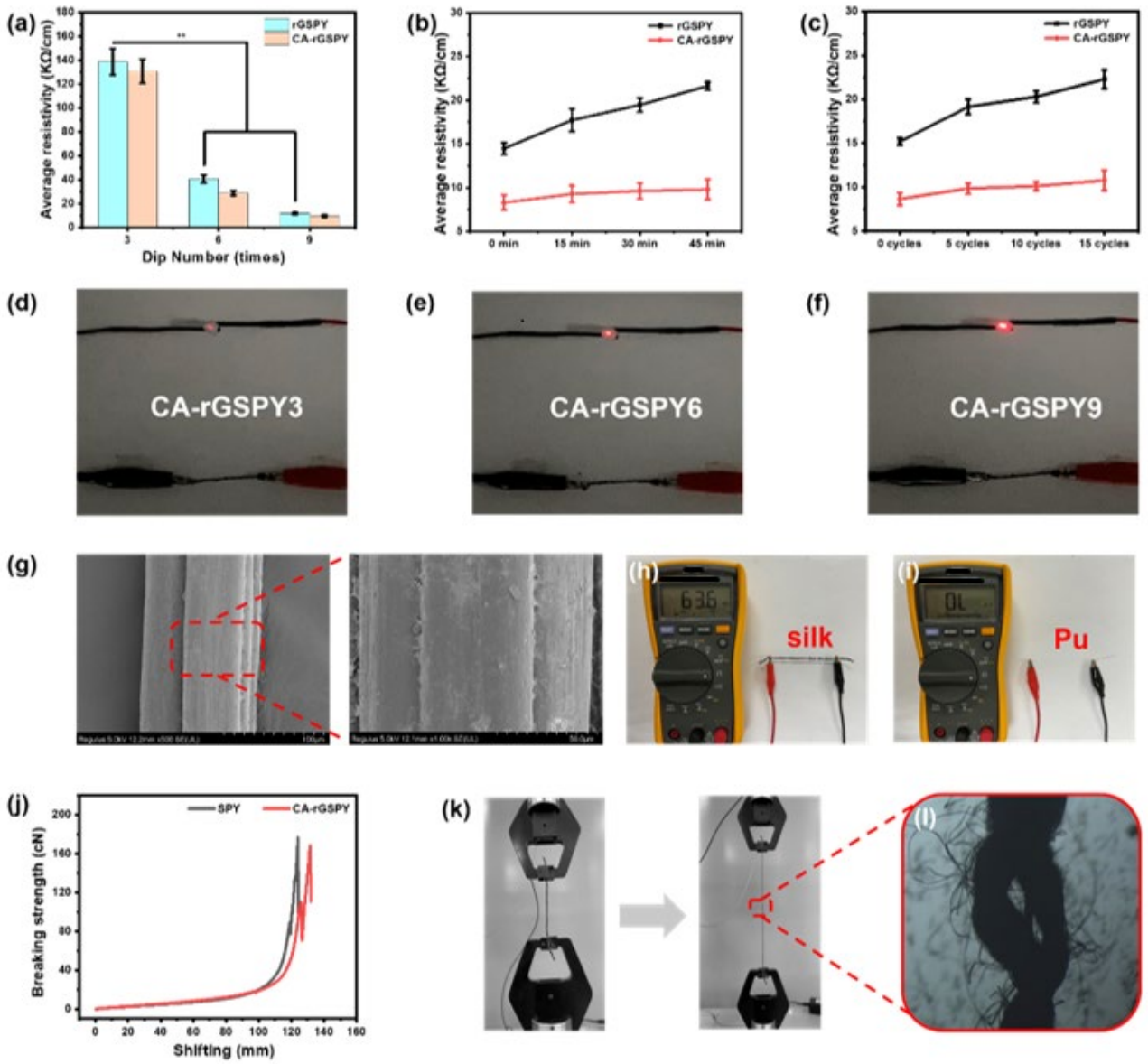

Fig. 3. Characterization of the CA-rGSPY. a) Average resistivity of the rGSPY and CA-rGSPY. The average resistivity of the rGSPY and CA-rGSPY after different b) washing time and c) washing cycles. The photographs of the d) CA-rGSPY3, e) CA-rGSPY6, and f) CA-rGSPY9 as an interconnect to light up LEDs. g) SEM images of the PU. h) Image of the silk with a resistance of 63.6 kΩ. i) Image of the PU with an unmeasurable resistance. j) The strain-stress curves of the SPY and CA-rGSPY9. k) The

images of the CA-rGSPY during stretching in a universal material testing machine. l) The image of the CA-rGSPY under high-deformation strain, showing the silk on the sheath layer starts to fracture.

3.2. Calibration and sensing mechanism of the CA-rGSPY sensor

Figure 4a shows the silk fibers wrapped in a spiral pattern with the PU yarn. Fig. 4b demonstrates the CA-rGSPY silk fibers exhibits outstanding tensile properties (with a maximum sensing range up to 120 %). An interesting observation is made from stretching the silk fibers as shown in Fig. 4c. The sensor exhibits a relatively linear decreasing resistance as a function of increasing strain and we denoted this behavior as the negative resistance response. This material property is extremely useful because the electrical response from the sensor is directly proportion with the electric current, which helps us to reduce the design complexity of the sensor structure. It should be noted that the increase in resistance is generally not favorable because it impacts the conductivity of sensors [40]. The CA-rGSPY3, CA-rGSPY6 and CA-rGSPY9 sensors possess outstanding linearity between the applied strain and the relative electrical variation. A goodness of fit, denoted as R^2, of CA-rGSPY3, CA-rGSPY6 and CA-rGSPY9 is shown to be 96.7 %, 99.2 % and 99.8 %, respectively. These results demonstrate that the slope of the linear fit increases as a function of coating cycles and the CA-rGSPY9 sensor offers better functional performance.

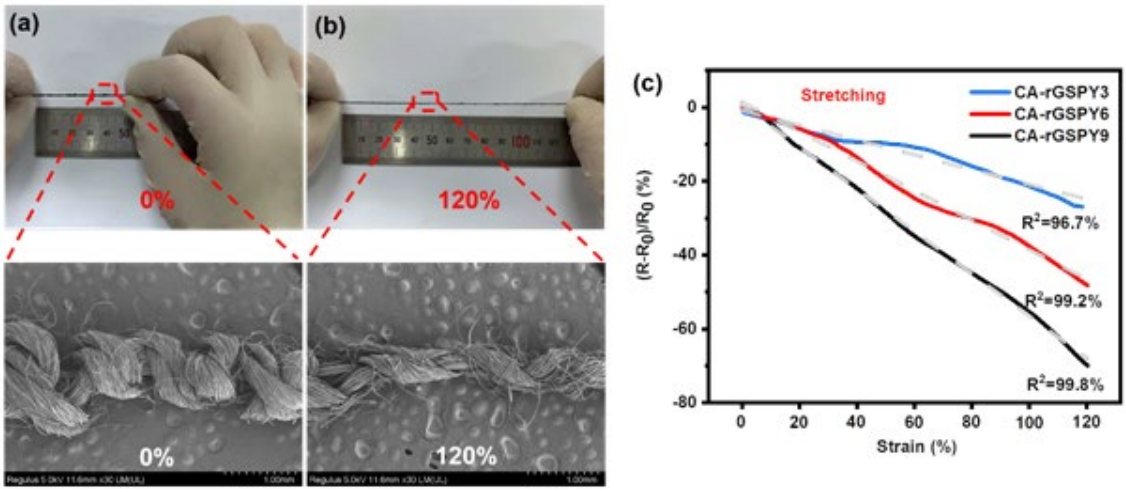

Fig. 4. Electrical responses and corresponding mechanism of the CA-rGSPY sensor under stretching. The images of the CA-rGSPY sensors under a) 0% elongation, and b) 120% elongation. c) The calibration results of the CA-rGSPY3, CA-rGSPY6 and CA-rGSPY9 sensors.

3.3. Electromechanical performance

The CA-rGSPY sensor reveals desirable electromechanical properties. We investigate the electrical response of the CA-rGSPY sensor under cyclic loading-unloading with various frequency and strain conditions. Fig. 5a shows the electrical outputs with the application of step-by-step frequency ranging from 0.1 Hz to 1 Hz at ~ 10 % strain. It can be seen that the sensor is capable of reliably detecting the applied strain at different frequencies. For dynamic strain conditions, strains ranging from 5 % to 50 % at a frequency of ~ 0.2 Hz are applied. Fig. 5b shows that the sensor is responsive to these dynamic conditions and the obtained signals are stable. However, it should be noted that the peak of the electrical response is slightly distorted at around 50 % strain and this is attributed to the hysteresis caused by the viscoelasticity of the PU material [7]. When the strain exceeds 50 %, the yarn is in slack state and it is unable to recover from the initial length within a short time. For that, there is a fluctuation in the sensor electrical signal at the beginning of the next cycle. By applying different tensile strains (i.e., 20 %, 40 % and 60 %) and retaining the elongation, the sensor generates signals corresponding

to the real-time perception capacity and this is shown in Fig. 5c.

We assess the response speed of the CA-rGSPY sensor by applying a quasi-transient step strain of ~ 0.5 % with a changing length speed of ~ 16 mm/s. Fig. 5d shows that the response time is approximately 80 ms which is fast enough to meet the most application requirements in body area motion detection. To further evaluate the stability and durability of the sensor, 50 % cyclic strain is applied with a frequency of ~ 0.5 Hz for 1500 cycles. Fig. 5e shows that the electrical response is stable throughout the cycle with minor fluctuation where the sensor is proven to be durability and has strong resistance in elastic fatigue. Additional studies are conducted; the CA-rGSPY sensor is washed with laundry solution for 30 min at ambient temperature and the results also reveal that the affect from laundry to the sensitivity of the sensor is relatively small. This observation suggests that the sensor will continue to work even subjected to different practical use scenarios.

Understanding the sensor behaviors at the wearable interface from various changing localized conditions in temperature and humidity (denoted as microclimate) is important for wearable sensors. Fig. 5f and 5g presents the use of an air-blower and a humidifier to adjust the temperature and the humidify, respectively, to mimic the changing conditions in real-world wearable scenarios. Fig. 5h shows the transient sensor electrical response as a function of increasing temperature (from ~ 25 °C to 45 °C) under cyclic loading strain of about 10 % and Fig. 5i shows the sensor total resistance. It can be seen that the change of temperature has minimal effects on the sensor response and the electrical property. A similar observation is shown in Fig. 5j and 5k where the relative humidity changes from 25 % to 60 %. This consistent sensor behavior in different microclimate conditions is ascribed to the

use of CA, where it helps to remove the oxygen-containing functional groups, and the process of GO reduction. These two processes facilitate small activated deep trap states and short-range variable hopping of carriers which leads to a dramatic decrease in the quantity of hopping charge transport (see Fig. 5l) [41, 42]. Therefore, although the increase in temperature can promote the generation of charge carriers, it is absent from temperature dependence because the number of hopping charges is reduced (see Fig. 5m) [43]. Meanwhile, the rGO presents high hydrophobicity due to the elimination of oxygen-containing functional groups including hydroxyl and carboxyl groups through the reduction process [12, 44]. Hence, the sensor can stably detect the tensile strain in the considered range of practical microclimates. It can be seen that the CA-rGSPY sensor has combined merits including negative resistance response, high linear sensing feature, high durability, and sensing reliability in varying temperature and humidity which can be provided as a cutting-edge wearable strain sensor.

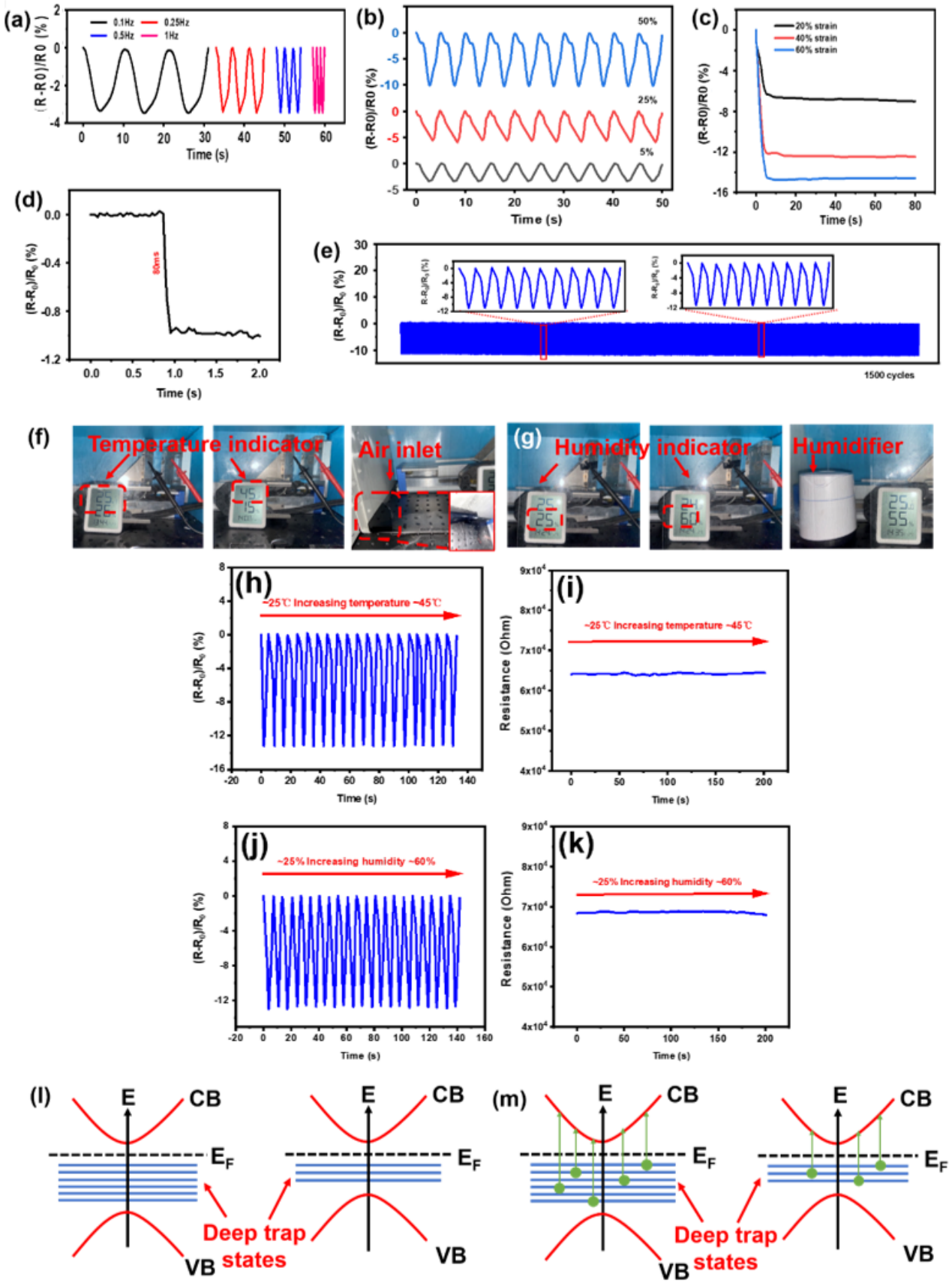

Fig. 5. Electromechanical properties of the CA-rGSPY sensor. a) Dynamic stability of the sensor at various frequencies ranging from 0.1 Hz to 1 Hz. b) Dynamic stability of the sensor at various strains

ranging from 5% to 50%. c) Static stability of the sensor at various strains ranging from 20% to 60%. d) The electrical signals by applying a quasi-transient step strain of 0.5% with a speed of 16 mm/s, showing the response speed. e) Electrical signals at an applied cyclic strain of 50% with a frequency of 0.5 Hz for 1500 cycles. The images of a homemade device for the evaluation of f) temperature and g) relative humidity dependence of the sensor. Electrical signals of the sensor under h) repeated loading strain of 10%, and i) undeformed conditions by applying changeable temperatures from 25-45°C, showing the sensor is insensitive to the temperature. Electrical signals of the sensor under j) repeated loading strain of 10%, and k) undeformed conditions by applying relative humidity from 25-60%, showing the sensor is insensitive to the humidity. l) Energy-band structure of the sensor with more and less oxygen-containing functional groups. m) Energy-band structure and thermal generation of charge carriers in the sensor with more and less oxygen-containing functional groups under changeable temperature.

3.5. Applications

A real-time body sensing network is developed and it is integrated with the CA-rGSPY strain sensor and a wireless data collection system. Fig. 6a shows the Bluetooth data collection system that is constructed with a Microprogrammed Control Unit (MCU), a Bluetooth serial port transparent transmission module (TM), an Analog to Digital Converter (ADC), and an antenna. To make it easier to understand how the system works, Fig. 6b illustrates a simple diagram. The system is powered by a 3.0 V power supply and the output signals of the CA-rGSPY sensor are amplified through an amplifier. The analog signal of each channel is then converted to a digital signal by the built-in 12-bit ADC. For data transfer, the system transmits signals wirelessly through a 2.4 GHz antenna. Ultimately, the electrical signals are sent to the mobile phone, which can be used to view the signals in real time (see Fig. 6c).

Five types of body motions, including coughing, speaking, drinking water, bending wrist, and breathing, are considered to demonstrate the robustness of the CA-rGSPY and the sensing network. By attaching the sensor to throat area with tape, epidermal vibrations generated from cough, speech,

and water drinking can be accurately monitored. Fig. 6d shows the sensor electrical response of coughing. Fig. 6e presents the electrical signals generated from speaking various words and Fig. 6f shows the electrical responses from drinking water. For example, the sensor can be attached on the skin of the wrist and Fig. 6a shows electrical signals from bending the wrist. By mounting the sensor on the chest, the generated electrical signals from Fig. 6h shows the motions due to inhalation and exhalation. As seen, the patterns of each of these signals are rather unique and it is believed that the sensing network with the CA-rGSPY sensor can be potentially used in pronunciation rehabilitation application, future personalized healthcare, and public health management.

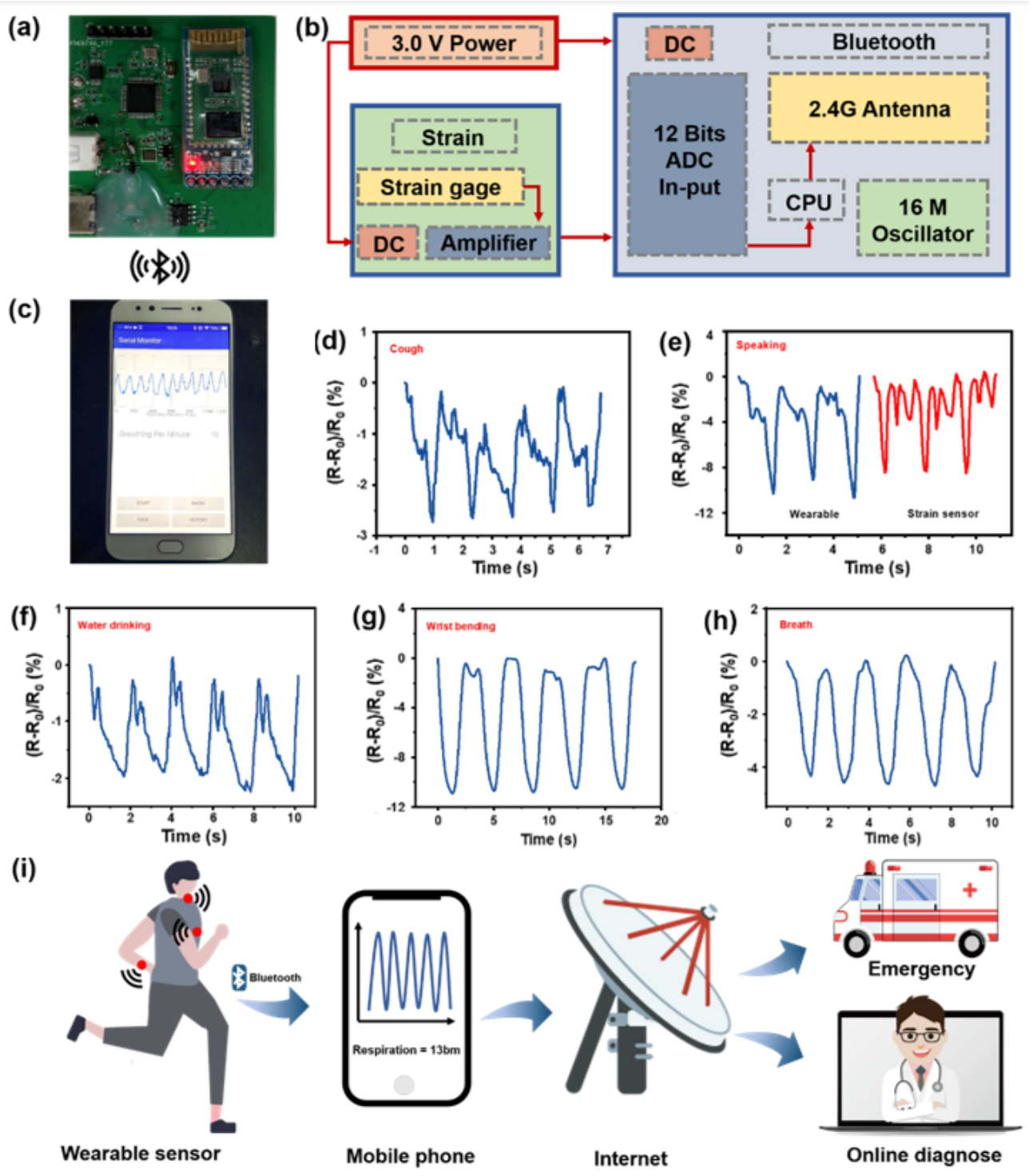

Fig. 6. Applications of the CA-rGSPY sensor in body area sensing networks. a) Circuit boards for signal conditioning and transmitting. b) The circuit diagram of the wireless transmission system. c) A mobile phone showing physiological data in digital form. d) Ream-time detection of coughing, e) speaking, and f) water drinking by attaching the sensor to the throat. g) Detection of the wrist bending through mounting the sensor on the wrist. h) Real-time detection of breathing by attaching the sensor to the chest. i) Proof-of-concept demonstration of remote and personalized sensing system based on the wearable sensor and data analysis and diagnosis system.

As a proof-of-concept for future activity monitoring and health management, Fig. 6i shows how the body sensing network can be used data collection, data transmission, data visualization, and abnormal event detections and warnings. The sensors, deployed to the elderly or apoplectic, can be used as mobility assistive devices capturing movement data to monitor the effectiveness of domestic rehabilitation interventions. The data of the care recipient are transmitted to a mobile phone and then relay to a remote terminal through the Internet. Emergency circumstances are detectable and emergency service can be delivered or provided immediately. In another case, medical care personnel can remotely examine a patient's status and perform an online diagnosis. Such a system presents unprecedented opportunities to revolutionize digital activity monitoring and health management in the future.

4. Conclusions

In summary, we have developed a wearable strain sensor with a core-sheath structure modified by graphene with the assistance of 3-glycidyloxypropyl trimethoxy silane as a CA. It exhibits enhanced sensitivity as a function of increased coating time and linear sensing feature (R^2 = 99.8 %) throughout the considered range of microclimates. The sensor coated nine times with graphene acquires a good electromechanical performance including fast response (i.e., 80 ms) and remarkable durability (>1500 cycles). Particularly, the sensor shows sensing reliability without the interference of changeable temperature from 25 °C to 45 °C, and relative humidity from 25 % to 60 %. We demonstrate a body area sensing network constructed by the sensor and a wireless signal collection system, which shows tremendous foreground in personal and public digital health management.

Declaration of Competing Interest

The authors declare that they have no known competing financial interests or personal relationships that could have appeared to influence the work reported in this paper.

References

[1] Y. Song, J. Min, Y. Yu, H. Wang, Y. Yang, H. Zhang, W. Gao, Wireless battery-free wearable sweat sensor powered by human motion, SCI ADV 6 (2020) eaay9842. https://doi.org/10.1126/sciadv.aay9842.

[2] M. Ku, J.C. Hwang, B. Oh, J.-U. Park, Smart Sensing Systems Using Wearable Optoelectronics, AISY. 2 (2020) 1900144. https://doi.org/https://doi.org/10.1002/aisy.201900144.

[3] K. Kwon, J.U. Kim, Y. Deng, S.R. Krishnan, J. Choi, H. Jang, K. Lee, C.-J. Su, I. Yoo, Y. Wu, L. Lipschultz, J.-H. Kim, T.S. Chung, D. Wu, Y. Park, T.-i. Kim, R. Ghaffari, S. Lee, Y. Huang, J.A. Rogers, An on-skin platform for wireless monitoring of flow rate, cumulative loss and temperature of sweat in real time, Nat. Electron. 4 (2021) 302-312. https://doi.org/10.1038/s41928-021-00556-2.

[4] Y. Yi, C. Yu, H. Zhai, L. Jin, D. Cheng, Y. Lu, Z. Chen, L. Xu, J. Li, Q. Song, P. Yue, Z. Liu, Y. Li, A free-standing humidity sensor with high sensing reliability for environmental and wearable detection, Nano Energy 103 (2022) 107780. https://doi.org/https://doi.org/10.1016/j.nanoen.2022.107780.

[5] S. Li, X. Xiao, J. Hu, M. Dong, Y. Zhang, R. Xu, X. Wang, J. Islam, Recent Advances of Carbon-Based Flexible Strain Sensors in Physiological Signal Monitoring, ACS Appl. Electron. Mater. 2 (2020) 2282-2300. https://doi.org/10.1021/acsaelm.0c00292.

[6] Z. Liu, T. Zhu, J. Wang, Z. Zheng, Y. Li, J. Li, Y. Lai, Functionalized Fiber-Based Strain Sensors: Pathway to Next-Generation Wearable Electronics, Nano-Micro Lett. 14 (2022) 61. https://doi.org/10.1007/s40820-022-00806-8.

[7] Z. Liu, Y. Zheng, L. Jin, K. Chen, H. Zhai, Q. Huang, Z. Chen, Y. Yi, M. Umar, L. Xu, G. Li, Q. Song, P. Yue, Y. Li, Z. Zheng, Highly Breathable and Stretchable Strain Sensors with Insensitive Response to Pressure and Bending, Adv. Funct. Mater. 31 (2021) 2007622. https://doi.org/https://doi.org/10.1002/adfm.202007622.

[8] C. Wang, K. Xia, H. Wang, X. Liang, Z. Yin, Y. Zhang, Advanced Carbon for Flexible and Wearable Electronics, Adv. Mater. 31 (2019) 1801072. https://doi.org/https://doi.org/10.1002/adma.201801072.

[9] Z. Wang, Y. Huang, J. Sun, Y. Huang, H. Hu, R. Jiang, W. Gai, G. Li, C. Zhi, Polyurethane/Cotton/Carbon Nanotubes Core-Spun Yarn as High Reliability Stretchable Strain Sensor for Human Motion Detection, ACS Appl. Mater. Interfaces 8 (2016) 24837-24843. https://doi.org/10.1021/acsami.6b08207.

[10] H. Park, Y.R. Jeong, J. Yun, S.Y. Hong, S. Jin, S.-J. Lee, G. Zi, J.S. Ha, Stretchable Array of Highly Sensitive Pressure Sensors Consisting of Polyaniline Nanofibers and Au-Coated Polydimethylsiloxane Micropillars, ACS Nano 9 (2015) 9974-9985. https://doi.org/10.1021/acsnano.5b03510.

[11] L. Xu, Z. Liu, H. Zhai, X. Chen, R. Sun, S. Lyu, Y. Fan, Y. Yi, Z. Chen, L. Jin, J. Zhang, Y. Li, T.T. Ye, Moisture-Resilient Graphene-Dyed Wool Fabric for Strain Sensing, ACS Appl. Mater. Interfaces 12 (2020) 13265-13274. https://doi.org/10.1021/acsami.9b20964.

[12] J. Zhang, J. Liu, Z. Zhao, D. Huang, C. Chen, Z. Zheng, C. Fu, X. Wang, Y. Ma, Y. Li, Z. Liu, Y. Li, G. Li, A facile scalable conductive graphene-coated Calotropis gigantea yarn, Cellulose 29 (2022) 3545-3556. https://doi.org/10.1007/s10570-022-04475-z.

[13] J.J. Park, W.J. Hyun, S.C. Mun, Y.T. Park, O.O. Park, Highly Stretchable and Wearable Graphene Strain Sensors with Controllable Sensitivity for Human Motion Monitoring, ACS Appl. Mater. Interfaces 7 (2015) 6317-6324. https://doi.org/10.1021/acsami.5b00695.

[14] Y. Ji, Y. Li, G. Chen, T. Xing, Fire-resistant and highly electrically conductive silk fabrics fabricated with reduced graphene oxide via dry-coating, Mater. Des. 133 (2017) 528-535. https://doi.org/https://doi.org/10.1016/j.matdes.2017.08.006.

[15] T. Yan, Z. Wang, Y.-Q. Wang, Z.-J. Pan, Carbon/graphene composite nanofiber yarns for highly sensitive strain sensors, Mater. Des. 143 (2018) 214-223. https://doi.org/https://doi.org/10.1016/j.matdes.2018.02.006.

[16] H. Montazerian, A. Rashidi, A. Dalili, H. Najjaran, A.S. Milani, M. Hoorfar, Graphene-Coated Spandex Sensors Embedded into Silicone Sheath for Composites Health Monitoring and Wearable Applications, Small 15 (2019) 1804991. https://doi.org/https://doi.org/10.1002/smll.201804991.

[17] X. Li, T. Hua, B. Xu, Electromechanical properties of a yarn strain sensor with graphene-sheath/polyurethane-core, Carbon 118 (2017) 686-698. https://doi.org/https://doi.org/10.1016/j.carbon.2017.04.002.

[18] Z. Liu, K. Chen, A. Fernando, Y. Gao, G. Li, L. Jin, H. Zhai, Y. Yi, L. Xu, Y. Zheng, H. Li, Y. Fan, Y. Li, Z. Zheng, Permeable graphited hemp fabrics-based, wearing-comfortable pressure sensors for monitoring human activities, Chem. Eng. J. 403 (2021) 126191. https://doi.org/https://doi.org/10.1016/j.cej.2020.126191.

[19] Z. Liu, Z. Li, Y. Yi, L. Li, H. Zhai, Z. Lu, L. Jin, J.R. Lu, S.Q. Xie, Z. Zheng, Y. Li, J. Li, Flexible strain sensing percolation networks towards complicated wearable microclimate and multi-direction mechanical inputs, Nano Energy 99 (2022) 107444. https://doi.org/https://doi.org/10.1016/j.nanoen.2022.107444.

[20] C. Wang, X. Li, E. Gao, M. Jian, K. Xia, Q. Wang, Z. Xu, T. Ren, Y. Zhang, Carbonized Silk Fabric for Ultrastretchable, Highly Sensitive, and Wearable Strain Sensors, Adv. Mater. 28 (2016) 6640-6648. https://doi.org/https://doi.org/10.1002/adma.201601572.

[21] S. Afroj, N. Karim, Z. Wang, S. Tan, P. He, M. Holwill, D. Ghazaryan, A. Fernando, K.S. Novoselov, Engineering Graphene Flakes for Wearable Textile Sensors via Highly Scalable and Ultrafast Yarn Dyeing Technique, ACS Nano 13 (2019) 3847-3857. https://doi.org/10.1021/acsnano.9b00319.

[22] Z. Tang, S. Jia, F. Wang, C. Bian, Y. Chen, Y. Wang, B. Li, Highly Stretchable Core–Sheath Fibers via Wet-Spinning for Wearable Strain Sensors, ACS Appl. Mater. Interfaces 10 (2018) 6624-6635. https://doi.org/10.1021/acsami.7b18677.

[23] Z. Tang, S. Jia, X. Shi, B. Li, C. Zhou, Coaxial Printing of Silicone Elastomer Composite Fibers for Stretchable and Wearable Piezoresistive Sensors, Polymers, 2019.

[24] L. Zulan, L. Zhi, C. Lan, C. Sihao, W. Dayang, D. Fangyin, Reduced Graphene Oxide Coated Silk Fabrics with Conductive Property for Wearable Electronic Textiles Application, Adv. Electron. Mater. 5 (2019) 1800648. https://doi.org/https://doi.org/10.1002/aelm.201800648.

[25] H. Zhai, L. Xu, Z. Liu, L. Jin, Y. Yi, J. Zhang, Y. Fan, D. Cheng, J. Li, X. Liu, Q. Song, P. Yue, Y. Li, Twisted graphene fibre based breathable, wettable and washable anti-jamming strain sensor for underwater motion sensing, Chem. Eng. J. 439 (2022) 135502. https://doi.org/https://doi.org/10.1016/j.cej.2022.135502.

[26] L.S. Connell, L. Gabrielli, O. Mahony, L. Russo, L. Cipolla, J.R. Jones, Functionalizing natural polymers with alkoxysilane coupling agents: reacting 3-glycidoxypropyl trimethoxysilane with poly(gamma-glutamic acid) and gelatin, Polym. Chem. 8 (2017) 1095-1103. https://doi.org/10.1039/c6py01425a.

[27] S. Palaskar, K.H. Kale, G.S. Nadiger, A.N. Desai, Dielectric barrier discharge plasma induced surface modification of polyester/cotton blended fabrics to impart water repellency using HMDSO, J.

Appl. Polym. Sci. 122 (2011) 1092-1100. https://doi.org/https://doi.org/10.1002/app.34237.

[28] L. Yang, H. Jiang, Y. Shen, L. Zhou, Antireflection coating on silk fabric fabricated from reactive silica nanoparticles and its deepening color performance, J. Sol-Gel Sci. Technol. 74 (2015) 488-498. https://doi.org/10.1007/s10971-015-3624-5.

[29] A.B. Giasuddin, D.W. Britt, Microwave Assisted Sol-Gel Synthesis of Silica-Spider Silk Composites, Molecules 24(14) (2019). https://doi.org/10.3390/molecules24142521.

[30] S. Bhattacharjee, C.R. Macintyre, P. Bahl, U. Kumar, X. Wen, K.-F. Aguey-Zinsou, A.A. Chughtai, R. Joshi, Reduced Graphene Oxide and Nanoparticles Incorporated Durable Electroconductive Silk Fabrics, Adv. Mater. Interfaces 7 (2020) 2000814. https://doi.org/https://doi.org/10.1002/admi.202000814.

[31] G. Cai, Z. Xu, M. Yang, B. Tang, X. Wang, Functionalization of cotton fabrics through thermal reduction of graphene oxide, Appl. Surf. Sci. 393 (2017) 441-448. https://doi.org/https://doi.org/10.1016/j.apsusc.2016.10.046.

[32] L.L. Xu, Z.K. Liu, H. Zhai, X. Chen, R.J. Sun, S.D. Lyu, Y.Y. Fan, Y.P.Q. Yi, Z.D. Chen, L. Jin, J.B. Zhang, Y. Li, T.T. Ye, Moisture-Resilient Graphene-Dyed Wool Fabric for Strain Sensing, ACS Appl. Mater. Interfaces 12 (2020) 13265-13274. https://doi.org/10.1021/acsami.9b20964.

[33] M. Fang, X. Xiong, Y. Hao, T. Zhang, H. Wang, H.-M. Cheng, Y. Zeng, Preparation of highly conductive graphene-coated glass fibers by sol-gel and dip-coating method, J. Mater. Sci. Technol. 35 (2019) 1989-1995. https://doi.org/https://doi.org/10.1016/j.jmst.2019.05.027.

[34] B. Li, J. Luo, X. Huang, L. Lin, L. Wang, M. Hu, L. Tang, H. Xue, J. Gao, Y.-W. Mai, A highly stretchable, super-hydrophobic strain sensor based on polydopamine and graphene reinforced nanofiber composite for human motion monitoring, Composites, Part B 181 (2020) 107580. https://doi.org/https://doi.org/10.1016/j.compositesb.2019.107580.

[35] S. Midha, R. Tripathi, H. Geng, P.D. Lee, S. Ghosh, Elucidation of differential mineralisation on native and regenerated silk matrices, Mater. Sci. Eng. C 68 (2016) 663-674. https://doi.org/https://doi.org/10.1016/j.msec.2016.06.041.

[36] Z.L. Liu, Z. Li, L. Cheng, S.H. Chen, D.Y. Wu, F.Y. Dai, Reduced Graphene Oxide Coated Silk Fabrics with Conductive Property for Wearable Electronic Textiles Application, Adv. Electron. Mater. 5 (2019) 9. https://doi.org/10.1002/aelm.201800648.

[37] C. Li, S. Yang, Y. Guo, H. Huang, H. Chen, X. Zuo, Z. Fan, H. Liang, L. Pan, Flexible, multi-functional sensor based on all-carbon sensing medium with low coupling for ultrahigh-performance strain, temperature and humidity sensing, Chem. Eng. J. 426 (2021) 130364. https://doi.org/https://doi.org/10.1016/j.cej.2021.130364.

[38] C. Li, D. Zhang, C. Deng, P. Wang, Y. Hu, Y. Bin, Z. Fan, L. Pan, High performance strain sensor based on buckypaper for full-range detection of human motions, Nanoscale 10 (2018) 14966-14975. https://doi.org/10.1039/C8NR02196A.

[39] J.J. Pan, M.Y. Yang, L. Luo, A.C. Xu, B. Tang, D.S. Cheng, G.M. Cai, X. Wang, Stretchable and Highly Sensitive Braided Composite Yarn@Polydopamine@Polypyrrole for Wearable Applications, ACS Appl. Mater. Interfaces 11 (2019) 7338-7348. https://doi.org/10.1021/acsami.8b18823.

[40] M. Zhang, M. Wang, M. Zhang, Q. Gao, X. Feng, Y. Zhang, J. Hu, G. Wu, Stretchable conductive Ni@Fe3O4@Polyester fabric strain sensor with negative resistance variation and electromagnetic interference shielding, Org. Electron. 81 (2020) 105677. https://doi.org/https://doi.org/10.1016/j.orgel.2020.105677.

[41] G. Eda, C. Mattevi, H. Yamaguchi, H. Kim, M. Chhowalla, Insulator to Semimetal Transition in Graphene Oxide, J. Phys. Chem. C 113 (2009) 15768-15771. https://doi.org/10.1021/jp9051402.

[42] T.Q. Trung, T.M.L. Dang, S. Ramasundaram, P.T. Toi, S.Y. Park, N.-E. Lee, A Stretchable Strain-Insensitive Temperature Sensor Based on Free-Standing Elastomeric Composite Fibers for On-Body Monitoring of Skin Temperature, ACS Appl. Mater. Interfaces 11 (2019) 2317-2327. https://doi.org/10.1021/acsami.8b19425.

[43] X.-Y. Fang, X.-X. Yu, H.-M. Zheng, H.-B. Jin, L. Wang, M.-S. Cao, Temperature- and thickness-dependent electrical conductivity of few-layer graphene and graphene nanosheets, Phys. Lett. A 379 (2015) 2245-2251. https://doi.org/https://doi.org/10.1016/j.physleta.2015.06.063.

[44] I.K. Moon, J. Lee, R.S. Ruoff, H. Lee, Reduced graphene oxide by chemical graphitization, Nat. Commun. 1 (2010) 73. https://doi.org/10.1038/ncomms1067.